This is a peer-reviewed, accepted author manuscript of the following article:
Wu, G., Zhao, B., Zhang, X., Wang, S., Egea-Àlvarez, A., Sun, Y. U., Li, Y., Guo, D., & Zhou, X. (Accepted/In press).
Impact of non-minimum-phase zeros on the weak-grid-tied VSC. IEEE Transactions on Sustainable Energy.

Impact of Non-minimum-phase Zeros on the Weak-Grid-Tied VSC

Guanglu Wu, Bing Zhao, Xi Zhang, *Member, IEEE*, Shanshan Wang, Agustí Egea-Àlvarez, *Member, IEEE*, Yuanyuan Sun, Yingbiao Li, Deyang Guo and Xiaoxin Zhou, *Fellow, IEEE*

***Abstract*—Right-half-plain (RHP) zeros can significantly deteriorate a control system's dynamic performances as it exhibits non-minimum-phase behaviors. In this paper, we investigate the occurrence mechanism of RHP zeros in weak-grid-tied VSCs as well as provide guidance for minimizing their effects. A reduced-order multi-input multi-output (MIMO) transfer function of the weak-grid-tied VSC is firstly obtained. Then, the single-input single-output (SISO) transfer function to study the impact of the RHP zeros on the power response is further derived. The existence of RHP zeros is examined by applying the Routh criterion on the numerator of the SISO open-loop transfer function. We find that RHP zeros can exist either when the VSC works as an inverter or a rectifier. Furthermore, large grid impedance values as well as operation points with high active power values can result in a non-minimum-phase system. It is also shown that RHP zeros limit the minimum PLL bandwidth. Simulation results and RTDS experiments validate the correctness of the analysis and the conclusions obtained.**

***Index Terms*—Weak-grid-tied VSC, non-minimum-phase zeros, MIMO transfer function, small-signal model, controller bandwidth**

I. Introduction

VOLTAGE source converters (VSCs) have been commonly used in the direct-drive permanent magnet synchronous generator (PMSG), the photovoltaic (PV) and the VSC based high voltage direct current transmission (VSC-HVDC) to transfer power in the AC grid [1], [2]. In spite of many advantages, there exist challenges when the VSC interfaces to a weak grid whose equivalent impedance is large [3]. These challenges include stability issues, poor dynamic margins, resonances and non-minimum phase characteristics, which can severely deteriorate the dynamic performance of the weak grid connected VSCs [4]–[7]. The non-minimum-phase characteristic influences the system significantly, as non-minimum-phase zeros limit the control bandwidth of the system [8].

The non-minimum-phase system usually refers to a system that has right half plane (RHP) zeros, i.e., non-minimum-phase zeros. The step response of a non-minimum-phase system usually has undershoot behaviors that the step response has a dip before it first gets to the reference value. Also, the RHP zero, z causes a large phase delay at the frequency $|z|$, and the system control bandwidth is usually limited below $|z|/2$ to ensure acceptable phase stability margins [8]. Zhang *et al.* reported the non-minimum-phase phenomena in the weak-grid-tied VSC system in [9], but in-depth study on the mechanism and impacts of the key parameters were not carried out. The difficulty to achieve a good control of a non-minimum-phase system highlights the necessity of a thorough investigation of the non-minimum-phase phenomena in weak-grid-tied VSCs. However, according to our knowledge, few research efforts have been devoted to this topic.

To analyze the RHP zeros of weak-grid-tied VSCs, a suitable model should be selected first. Till now, several models have been proposed to investigate the small-signal stability of the weak-grid-tied VSCs. Sun *et al.* [10], [11] proposed an impedance-based method for VSCs connecting to weak grids, indicating that the VSC-grid interconnections are stable when the ratio of the grid impedance to the inverter output impedance satisfies the Nyquist criterion [12]. Hu *et al.* [1], [13] proposed the complex-torque-based method to analyze the stability of the VSC that connects to a high-impedance AC grid, by analogy with the sub-synchronous oscillation analysis of synchronous generators [14]. Zhou *et al.* applies the eigenvalue analysis method to the stability analysis of the target system, and it can cast a full picture of the modal oscillation and the damping characteristics [3], [4], [15]–[17]. However, the eigenvalue analysis only focuses on the closed-loop poles. The impedance and complex torque method are also limited for providing insights into the RHP zeros.

One classical method that can be used to study the system's RHP zeros is the transfer function, whose numerator's roots are the zeros. In literature, transfer functions with high dimensions have been derived for studying grid-connected VSCs [18], [19]. However, the high dimension and intricacy limit the application of the transfer function-based method on investigating RHP zeros [9]. To overcome the limitation, the transfer function should be carefully simplified with appropriate dimension reduction. It is noticed that the non-minimum-phase phenomena are mainly related to the outer loop of the VSC. The time constant of the inner current loop is much faster than that of the outer loop. Some researchers suggested that the inner current loop dynamics can be neglected due to different time scales [20], [21].

This paper focuses on analyzing the non-minimum-phase phenomena of the weak-grid-tied VSC system using reduced-order transfer functions [19], [20]. Compared with the prior work [9], [19], [20], our paper provides an in-depth investigation of the underlying mechanism of the non-minimum-phase

Manuscript received March 2020. This work is supported by State Grid Corporation of China under Technology Project No. XT71-19-020: Research on the topology of the voltage source converter for Stand-alone Renewable Generation integration system. (*Corresponding Author: Xi Zhang*)

G. Wu, B. Zhao, S. Wang, D. Guo and X. Zhou are with State Key Laboratory of Power Grid Safety and Energy Conservation, China Electric Power Research Institute, Beijing, China, 100192.

X. Zhang is with the School of Automation and Key Laboratory for Intelligent Control and Decision on Complex Systems, Beijing Institute of Technology, Beijing 100081, China. (Email:xizhang@bit.edu.cn.)

A. Egea-Àlvarez is with Department of Electronic and Electrical Engineering, University of Strathclyde, 16 Richmond St, Glasgow G1 1XQ, U.K.

Y. Sun is with the Key Laboratory of Power System Intelligent Dispatch and Control, School of Electrical Engineering, Shandong University, Jinan 250061, China.

Y. Li is with the School of Electrical and Electronic Engineering, Huazhong University of Science and Technology, Wuhan, 430074, China.

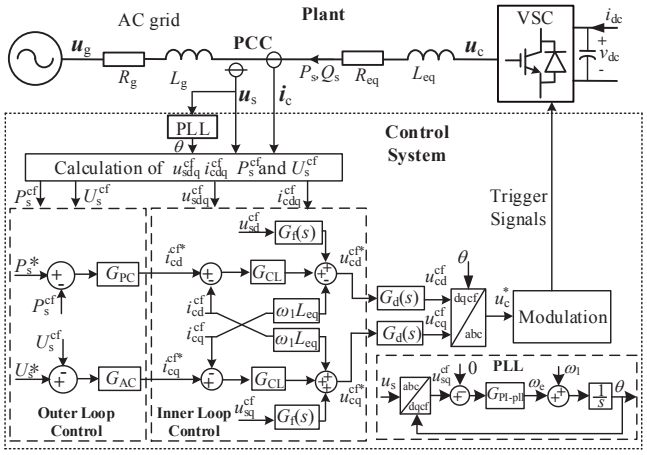

Fig. 1. A diagram of the target system where a VSC connects to a weak grid.

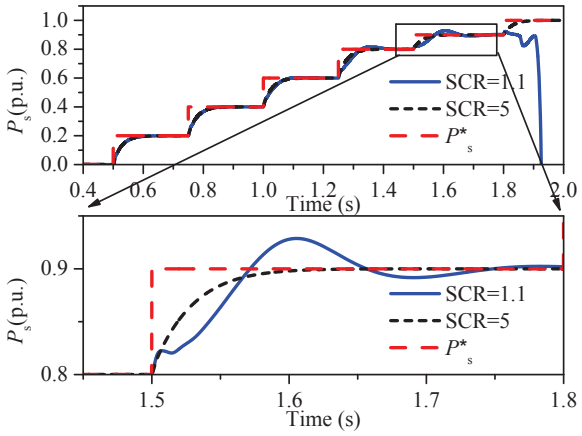

Fig. 2. Non-minimum-phase phenomena of the power step responses with SCR=1.1.

phenomena of the weak-grid-tied VSC using a simplified transfer function. We also provide a comprehensive control gain tuning recommendations for mitigating the RHP zeros effect based on the analytical study of the resulting transfer function. Firstly, Section II presents the weak-grid-tied VSC system and the non-minimum-phase phenomena observed. Secondly, the reduced-order multi-input multi-output (MIMO) transfer functions of the VSC system are obtained in Section III by neglecting the fast current control dynamics. In Section IV, the single-input single-output (SISO) transfer function for a specific input-output pair is obtained, and the Routh criterion is applied to examine the RHP zeros where the physical understanding of this phenomena is demonstrated. The impact of key system parameters on RHP zeros and the guidance for improving dynamic performance are discussed. In Sections V and VI, Simulink simulations and RTDS experiments are performed. Simulation results verify the correctness of our analysis on the non-minimum-phase phenomena and the efficacy of the guidance for the performance improvement.

II. Glimpse of the Non-minimum-phase System

In this section, we provide a glimpse of the weak-grid-tied VSC system and the non-minimum-phase phenomena observed.

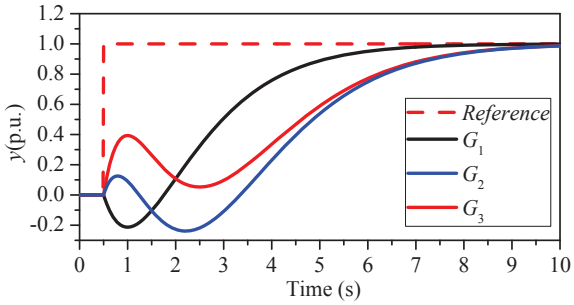

Fig. 3. Undershoot behaviors of the typical non-minimum-phase systems.

Fig. 1 shows the schematic of the typical scenario, where a VSC connects to a weak grid. The converter controller is composed by an inner loop, an outer loop and a PLL. The PLL provides the synchronization with the grid, the inner loop controls the active and reactive current through the converter line reactor and the outer loop generates references for the inner loop to control the power and the AC voltage magnitude [3], [4]. And $\boldsymbol{u}_g$, $\boldsymbol{u}_s$, $\boldsymbol{u}_c$ are the grid voltage, the PCC (point of common coupling) voltage and the VSC output voltage, $\boldsymbol{i}_c$ is the current injecting to the grid.

Fig. 2 shows the step responses of the input-output pair $P_s^* \sim P_s$ of the VSC when it connects to a grid with SCR=1.1 and a grid with SCR=5. It shows that the step response directly increases to its reference when SCR=5. While, the step response initially increases, then decreases, and finally increases to its reference when SCR=1.1, indicating that the grid-tied VSC is a non-minimum-phase system.

The open-loop transfer functions of three typical non-minimum-phase systems in [22] are as follows,

$$G_1 = \frac{-(s-1)}{(s+1)^2}, G_2 = \frac{(s-1)^2}{(s+1)^3}, G_3 = \frac{\left(2s^2 - s + 1\right)}{(s+1)^3}, \quad (1)$$

where G_1 has one positive RHP zero, G_2 has two positive RHP zeros, and G_3 has two non-real RHP zeros. And their step responses are shown in Fig. 3. The step responses of the three systems all exhibit undershoot (inverse response) behaviors, i.e., the step responses have dips before they first reach the reference values.

The step response of the VSC in Fig. 2 with SCR=1.1 is similar to that of G_3 in Fig. 3 that has two non-real RHP non-minimum-phase zeros. To understand the non-minimum-phase phenomena better and guide the performance improvement, we need to further obtain the transfer function of the target system, and explore the impacts of the key parameters on the existence of RHP zeros.

III. Transfer Functions of the Grid-Tied VSC System

In this section, we derive the simplified MIMO transfer function of the grid-tied VSC system, based on which the analysis of the non-minimum-phase phenomena can be performed. Due to the different time scales of the inner current loop and the outer loop, it is assumed that the inner current loop dynamics can be neglected, i.e., the current can track its reference instantaneously in the control system's dq synchronous frame [20], [21].

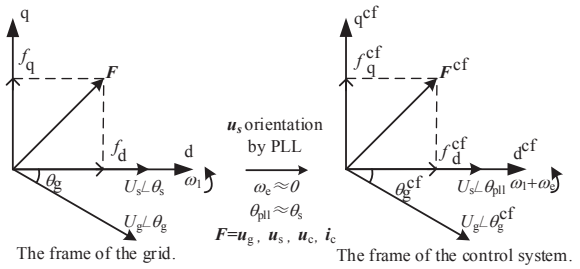

Fig. 4. The frames of the grid and the control system.

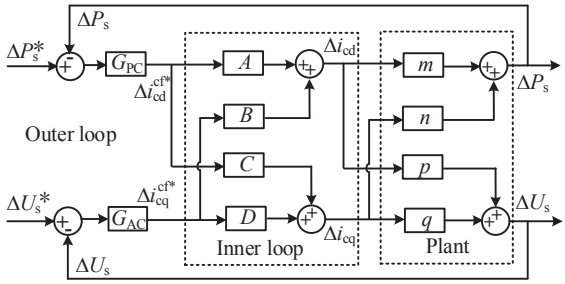

Fig. 5. Signal flow chart of the linear representation of the VSC system.

A. The Analytical MIMO Transfer Function

The grid and converter control modeling mathematical formulation can be seen in the Appendix. As the power converter is orientated using a PLL, two references frame will exist, one for the electrical network and one for the controller as shown in Fig. 4. The superscript "cf" denotes that the variable is in the the control system's dq synchronous frame.

The ω_e is the angular frequency difference between the two dq frames , and ω_1 is $2\pi 50$rad/s. Fig. 5 shows the block diagram of the linearized representation of the VSC system, which consists of the small-signal models of the plant, the inner loop and the outer loop.

From Figs. 1 and 5, the VSC has two inputs ΔP_s^*, ΔU_s^* and two outputs ΔP_s, ΔU_s. Thus, a MIMO (two-input-two-output) transfer function is required to describe the dynamics of the grid-tied VSC system.

The relationship between the outputs of ΔP_s, ΔU_s and the perturbations of Δi_{cd}, Δi_{cq} and Δi_{cd}^{cf*}, Δi_{cq}^{cf*} can be written as

$$\begin{bmatrix} \Delta P_s \\ \Delta U_s \end{bmatrix} = \begin{bmatrix} m & n \\ p & q \end{bmatrix} \begin{bmatrix} A & B \\ C & D \end{bmatrix} \begin{bmatrix} \Delta i_{cd}^{cf*} \\ \Delta i_{cq}^{cf*} \end{bmatrix}, \tag{2}$$

where m, n, p, and q are expressed as

$$\begin{cases} m = 1.5\left[u_{sd0}+i_{cq0}X_g+i_{cd0}R_g\right], p = 0 \\ n = 1.5\left[-i_{cd0}X_g+i_{cq0}R_g\right], q = -X_g \end{cases}, \tag{3}$$

where subscripts of d and q are the direct and quadrature-axis components in synchronous reference frame, the subscript 0 denotes steady-state value, i_c is the current injected to the PCC, u_s is the PCC voltage, u_g is the equivalent grid voltage, u_c is the output voltage of the VSC, R_g and X_g are the equivalent resistance and inductance of the AC grid respectively. A, B, C and D are described by

$$\begin{cases} A = \frac{1}{1+G_{pll}X_gI_{cq0}}, B = 0 \\ C = \frac{G_{pll}X_gI_{cd0}}{1+G_{pll}X_gI_{cq0}}, D = 1 \end{cases}, \tag{4}$$

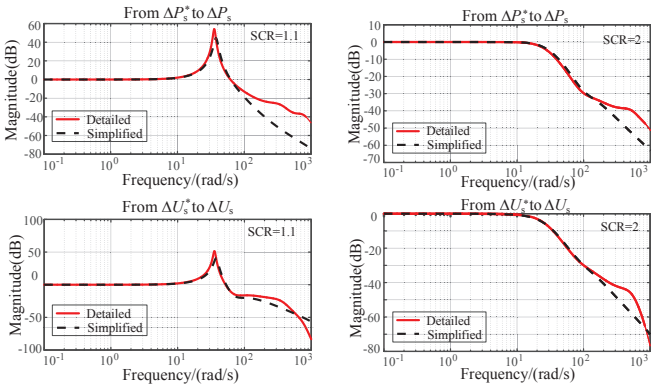

Fig. 6. Comparison of the magnitude-frequency responses of the detailed and the simplified models: SCR=1.1, SCR=2.

where G_{pll} is the transfer function of the PLL that is written as

$$G_{pll} = \frac{\left(2\zeta\omega_{pll}s + \omega_{pll}^2\right)/u_{sd0}}{s^2 + 2\zeta\omega_{pll}s + \omega_{pll}^2}. \tag{5}$$

where ζ is the damping ratio, ω_{pll} is the bandwidth of the PLL. The outer loop expressed in (30) can be linearized as

$$\begin{bmatrix} \Delta i_{cd}^{cf*} \\ \Delta i_{cq}^{cf*} \end{bmatrix} = \begin{bmatrix} G_{PC} & 0 \\ 0 & G_{AC} \end{bmatrix} \left(\begin{bmatrix} \Delta P_s^* \\ \Delta U_s^* \end{bmatrix} - \begin{bmatrix} \Delta P_s^{cf} \\ \Delta U_s^{cf} \end{bmatrix} \right), \tag{6}$$

where G_{PC} and G_{AC} are the PI controllers of the active power control and the AC voltage control. It can be proved that

$$\begin{cases} \Delta P_s^{cf} = \Delta P_s \\ \Delta U_s^{cf} = \Delta U_s \end{cases}. \tag{7}$$

Then, the MIMO transfer function can be obtained by substituting (6), (7) into (2),

$$\begin{bmatrix} \Delta P_s \\ \Delta U_s \end{bmatrix} = \begin{bmatrix} 1+X & Y \\ M & 1+N \end{bmatrix}^{-1} \begin{bmatrix} X & Y \\ M & N \end{bmatrix} \begin{bmatrix} \Delta P_s^* \\ \Delta U_s^* \end{bmatrix}, \tag{8}$$

where X, Y, M and N are short for the expressions of

$$\begin{cases} X = G_{PC}\left(mA + nC\right), Y = G_{AC}\left(mB + nD\right) \\ M = G_{PC}\left(pA + qC\right), N = G_{AC}\left(pB + qD\right) \end{cases}. \tag{9}$$

Also, equation (8) can be reformed and written as

$$\begin{bmatrix} \Delta P_s \\ \Delta U_s \end{bmatrix} = \begin{bmatrix} \frac{G_{PC0}}{1+G_{PC0}} & \frac{\frac{Y}{(1+X)}}{1+G_{AC0}} \\ \frac{\frac{M}{(1+N)}}{1+G_{PC0}} & \frac{G_{AC0}}{1+G_{AC0}} \end{bmatrix} \begin{bmatrix} \Delta P_s^* \\ \Delta U_s^* \end{bmatrix}, \tag{10}$$

where G_{PC0} and G_{AC0} can be described by

$$\begin{cases} G_{PC0} = X - \frac{YM}{(1+N)} \\ G_{AC0} = N - \frac{YM}{(1+X)} \end{cases}. \tag{11}$$

B. Model Verification

The magnitude-frequency responses of the MIMO transfer function in (10) and the original detailed model in Fig. 1 that built in the Matlab are compared with each other to validate its feasibility, as shown in Fig. 6 when SCR=1.1 and 2. The other parameters are the same with those in Table III in Section V. We can see that the magnitude-frequency curves of the simplified MIMO description and the detailed model match well with each other in the medium and low-frequency that above -3dB. Thus, the reduced-order transfer function is accurate enough for investigating the outer loop and the PLL related non-minimum-phase dynamics.

TABLE I
THE ROUTH TABLE

	1	2	3
$1(s^3)$	a_0	a_2	0
$2(s^2)$	a_1	a_3	0
$3(s^1)$	b_1	0	0
$4(s^0)$	c_1	0	0

IV. NON-MINIMUM-PHASE ZEROS ANALYSIS

In this section, we first obtain the SISO transfer function for a specific input-output pair. Then, by applying the Routh criterion on the numerator of the open-loop transfer function of the SISO representation, RHP zeros can be examined qualitatively. The physical understanding and inherent mechanism of non-minimum-phase behavior are demonstrated. The impacts of key system parameters on the RHP zeros and the guidance for the dynamic performance improvement are discussed.

A. SISO Transfer Functions for Specific Input-Output Pairs

From the MIMO transfer function shown in (10), we can see that there are 4 input-output pairs and can get 4 corresponding SISO transfer functions. Theoretically, the non-minimum-phase phenomena will occur when the system's transfer function has RHP zeros.

To be consistent with Fig. 2, we analyze the non-minimum-phase phenomena for the input-output pair $P_s^* \sim P_s$. From (10), the corresponding SISO transfer function can be derived as

$$\Delta P_s = \frac{G_{PC0}}{1+G_{PC0}} \Delta P_s^*, \tag{12}$$

where G_{PC0} is the open-loop transfer function. By substituting (4) and (9) into (11), G_{PC0} can be obtained as follows,

$$G_{PC0} = G_{PC} \frac{m}{1+G_{pll} X_g I_{cq0}} \left(1 + \frac{n}{1+G_{AC} q} \frac{G_{pll} X_g I_{cd0}}{m}\right). \tag{13}$$

The detailed expression of G_{PC0} is further shown in (15) by substituting (31) and (5) into (13), where ω_{OL_PC} is the bandwidth of the active power control, G_{PC0_1} presents the active power control and G_{PC0_2} contains the PLL, the AC voltage control, the AC system strength, and the active power. G_{AC2PC}, k_1, and k_2 in G_{PC0_2} are written as

$$\begin{cases} G_{AC2PC} = \dfrac{s}{1+s\left(T_{i\_AC} + \frac{1}{\omega_{OL\_AC}}\right)} \\ k_1 = \dfrac{X_g i_{cq0}}{u_{sd0}}, k_1 \in (-1, 1) \\ k_2 = \dfrac{1}{\omega_{OL\_AC}} \dfrac{-1.5(i_{cd0} X_g)^2}{u_{sd0} m} < 0 \end{cases}, \tag{14}$$

where ω_{OL_AC} is the bandwidth of the AC voltage control, T_{i_AC} is the integral time constant of G_{AC} and $T_{i\_AC} = 1/\omega_{CL}$, where ω_{CL} is the bandwidth of the inner loop control.

B. RHP Zeros Examination Based on the Routh Criterion

The non-minimum-phase phenomena will emerge when the open-loop transfer function G_{PC0} has RHP zeros. According to (15), the existence of RHP zeros of G_{PC0} depends on G_{PC0_2}, in that G_{PC0_1} has only one negative zero. The Routh criterion can be used to check whether G_{PC0_2} has RHP zeros. Table I shows the Routh table for equation $(a_0 s^3 + a_1 s^2 + a_2 s + a_3 = 0)$.

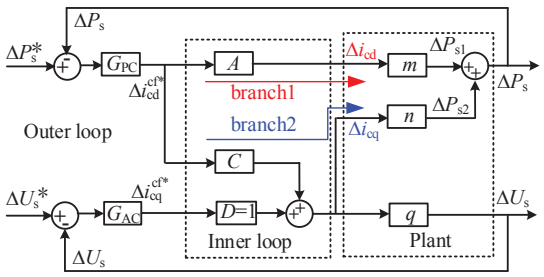

Fig. 7. Signal flow chart for the input-output pair $P_s^* \sim P_s$.

According to the Routh criterion, G_{PC0_2} has no RHP zeros if and only if it satisfies

$$a_0 > 0, a_1 > 0, a_2 > 0, a_3 > 0, b_1 > 0, c_1 > 0 \tag{17}$$

According to (16), $a_0 > 0$ and $a_3 = c_1 > 0$ are satisfied. Thus, (17) can be simplified to

$$a_1 > 0, a_2 > 0, b_1 = \frac{a_1 a_2 - a_0 a_3}{a_1} > 0 \tag{18}$$

The signs of a_1, a_2, and b_1 depend on k_2 once the control parameters are given. From (14), k_2 consists of the AC system strength (represented by X_g) and the active power (represented by i_{cd0}), indicating that the values of the AC system strength (SCR) and the active power play important roles in the formation of the non-minimum-phase system.

Also, the RHP zeros are not changed either the VSC works as a rectifier ($i_{cd0} < 0$) or an inverter ($i_{cd0} > 0$), in that the $X_g i_{cd0}$ in k_2 exists in the form of the squared value according to (14).

C. Physical Understandings of the Non-minimum-phase Phenomena

According to (14) and (16), the RHP zeros originate from the negative sign of k_2 and the large grid impedance (X_g). The negative sign of k_2 is determined by the coefficient of n in the linear model of the plant in (3).

Fig. 7 demonstrates the two signal flow branches for the input-output pair $P_s^* \sim P_s$. Branch 2 disappears in strong grid conditions, as C=0 and n=0. In weak grid conditions where $C \neq 0$ and $n < 0$, branch 2 leads to the non-minimum-phase phenomena.

By substituting the expressions of Δi_{cd} and Δi_{cq} into the plant's linear model $\Delta P_s = \Delta P_{s1} + \Delta P_{s2} = m\Delta i_{cd} + n\Delta i_{cq}$, the expression of ΔP_s is presented in (19) without the outer loops, where $m > 0$ and $n < 0$ according to (3). The undershoot behavior appears in the active power response because

1) an increase of the active current reference Δi_{cd}^{cf*} results in the increases of the current Δi_{cd} and the power ΔP_{s1}, as $\Delta P_{s1} = m\Delta i_{cd}$ where $m > 0$.

2) an increase of the active current reference Δi_{cd}^{cf*} results in an increase of the current Δi_{cq} and a decrease of the power ΔP_{s2}, as $\Delta P_{s2} = n\Delta i_{cq}$ where $n < 0$.

These are the inherent mechanisms that causes the undershoot behavior of the active power response in the converter dynamics. It can also be proved by (19) that the detailed expression of ΔP_{s1} has a positive sign, while the detailed

$$G_{\mathrm{PC0}}=\underbrace{\frac{\omega_{\mathrm{OL\_PC}}\left(sT_{\mathrm{i\_PC}}+1\right)}{s}}_{G_{\mathrm{PC0\_1}}}\times\underbrace{\frac{m}{1.5U_{\mathrm{sm}}}\frac{\left[\left(s^2+2\zeta\omega_{\mathrm{pll}}s+\omega_{\mathrm{pll}}^2\right)+\left(2\zeta\omega_{\mathrm{pll}}s+\omega_{\mathrm{pll}}^2\right)k_2G_{\mathrm{AC2PC}}\right]}{\left[\left(s^2+2\zeta\omega_{\mathrm{pll}}s+\omega_{\mathrm{pll}}^2\right)+\left(2\zeta\omega_{\mathrm{pll}}s+\omega_{\mathrm{pll}}^2\right)k_1\right]}}_{G_{\mathrm{PC0\_2}}} \tag{15}$$

$$G_{\mathrm{PC0\_2}}=\frac{m}{1.5U_{\mathrm{sm}}}\frac{\left(a_0s^3+a_1s^2+a_2s+a_3\right)}{\left[\left(s^2+2\zeta\omega_{\mathrm{pll}}s+\omega_{\mathrm{pll}}^2\right)+\left(2\zeta\omega_{\mathrm{pll}}s+\omega_{\mathrm{pll}}^2\right)k_1\right]\left(1+sT_{\mathrm{eq\_}AC}\right)},\ where\begin{cases}a_0=T_{\mathrm{eq\_}AC}=T_{\mathrm{i\_AC}}+1/\omega_{\mathrm{OL\_AC}}>0\\ a_1=1+\left(T_{\mathrm{eq\_AC}}+k_2\right)2\zeta\omega_{\mathrm{pll}}\\ a_2=2\zeta\omega_{\mathrm{pll}}+\left(T_{\mathrm{eq\_AC}}+k_2\right)\omega_{\mathrm{pll}}^2\\ a_3=\omega_{\mathrm{pll}}^2>0\end{cases} \tag{16}$$

$$\Delta P_s=\Delta P_{s1}+\Delta P_{s2}=m\Delta i_{\mathrm{cd}}+n\Delta i_{\mathrm{cq}}=mA\Delta i_{\mathrm{cd}}^{\mathrm{cf}*}+n\left(C\Delta i_{\mathrm{cd}}^{\mathrm{cf}*}+D\Delta i_{\mathrm{cq}}^{\mathrm{cf}*}\right)=\frac{\left(s^2+2\zeta\omega_{\mathrm{pll}}s+\omega_{\mathrm{pll}}^2\right)}{s^2+\left(2\zeta\omega_{\mathrm{pll}}s+\omega_{\mathrm{pll}}^2\right)(1+k_1)}m\Delta i_{\mathrm{cd}}^{\mathrm{cf}*}+\frac{\left(2\zeta\omega_{\mathrm{pll}}s+\omega_{\mathrm{pll}}^2\right)}{s^2+\left(2\zeta\omega_{\mathrm{pll}}s+\omega_{\mathrm{pll}}^2\right)(1+k_1)}k_3n\Delta i_{\mathrm{cd}}^{\mathrm{cf}*}+n\Delta i_{\mathrm{cq}}^{\mathrm{cf}*}$$
$$=\underbrace{\frac{\left(s^2+2\zeta\omega_{\mathrm{pll}}s+\omega_{\mathrm{pll}}^2\right)}{s^2+\left(2\zeta\omega_{\mathrm{pll}}s+\omega_{\mathrm{pll}}^2\right)\left(1+\frac{X_{\mathrm{g}}i_{\mathrm{cq0}}}{u_{\mathrm{sd0}}}\right)}1.5\left(u_{\mathrm{sd0}}+X_{\mathrm{g}}i_{\mathrm{cq0}}\right)\Delta i_{\mathrm{cd}}^{\mathrm{cf}*}}_{Branch1,\Delta P_{s1}:Overshoot}-\underbrace{\left[\frac{\left(2\zeta\omega_{\mathrm{pll}}s+\omega_{\mathrm{pll}}^2\right)}{s^2+\left(2\zeta\omega_{\mathrm{pll}}s+\omega_{\mathrm{pll}}^2\right)\left(1+\frac{X_{\mathrm{g}}i_{\mathrm{cq0}}}{u_{\mathrm{sd0}}}\right)}\frac{1.5(X_{\mathrm{g}}i_{\mathrm{cd0}})^2}{u_{\mathrm{sd0}}}\Delta i_{\mathrm{cd}}^{\mathrm{cf}*}+1.5X_{\mathrm{g}}i_{\mathrm{cd0}}\Delta i_{\mathrm{cq}}^{\mathrm{cf}*}\right]}_{Branch2,\Delta P_{s2}:Unershoot}, \tag{19}$$

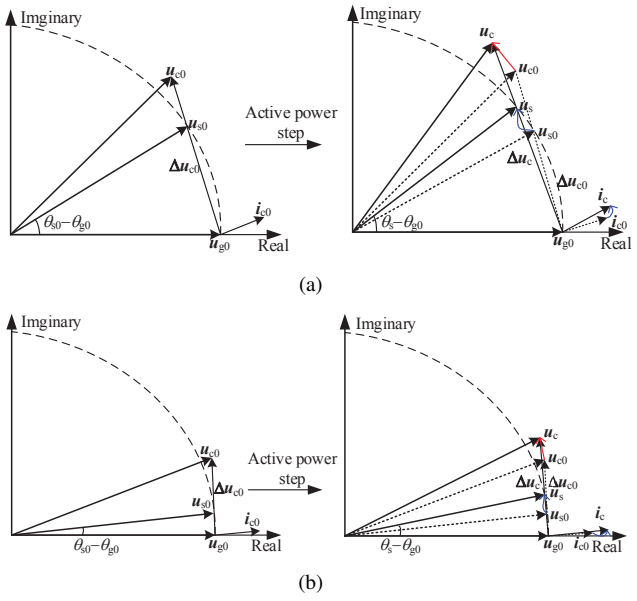

Fig. 8. Vector diagrams of the VSC before and after a step input is imposed. (a) The VSC connects to a weak grid; (b) The VSC connects to a strong grid.

expression of ΔP_{s2} has a negative sign, which results in the undershoot behavior.

Fig. 8 uses vector diagrams to display the voltages and currents in the VSC before and after a step input is imposed in weak and strong grid conditions, respectively. It is known that the voltage can change abruptly but the current across the impedance cannot. When there is a step of P_s^*, the output voltage of the VSC changes abruptly to force the active current to change. The large active current will lead to a voltage drop over the grid impedance, especially in weak grid conditions, see Fig. 8(a). Then the AC voltage control of the VSC will react to generate a reactive current to increase the AC voltage.

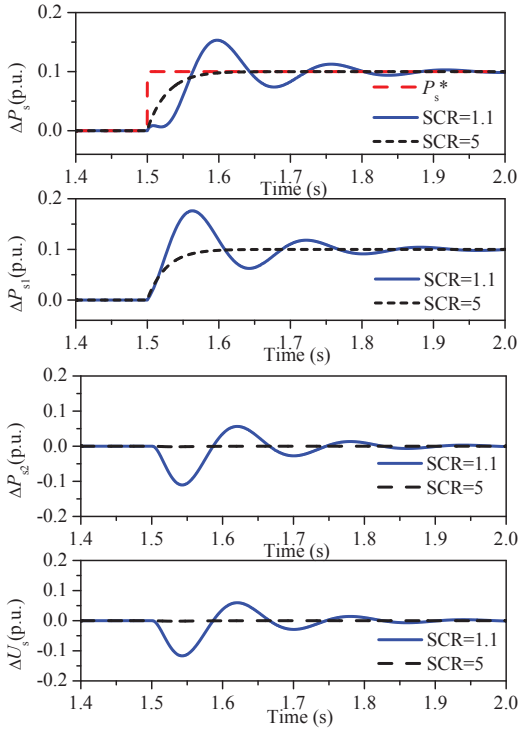

Fig. 9. Comparison of the step responses in Fig. 7 in weak and strong grid conditions, where ΔP_s is the total power step response, ΔP_{s1} is the power response in branch1, ΔP_{s2} is the power response in branch2, and ΔU_s is the voltage response.

The phasers converge to a new steady state after the dynamics. While, the voltage drop over the grid impedance is small enough to be neglected in strong grid conditions, see Fig. 8(b).

Fig. 9 shows the active power step responses of the linear model in Fig. 7 when P_s=0.85 p.u.. The other parameters are the same with those in Table III in Section V. In weak grid conditions, when there is a step input, the d-axis current

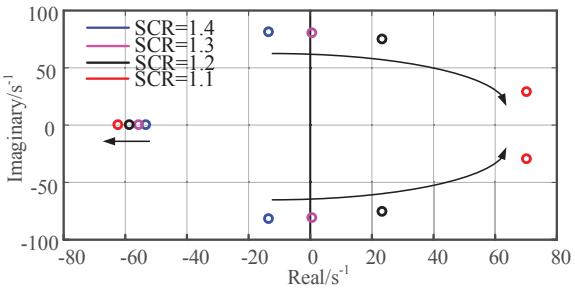

Fig. 10. Impact of the SCR on the zeros of G_{PC0_2}.

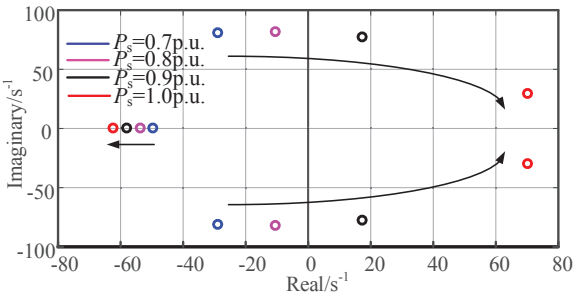

Fig. 11. Impact of the active power on the zeros of G_{PC0_2}.

reference will increase and produce a power increase in branch 1, see ΔP_{s1} in Fig. 9. At the same time, the q-axis current in branch 2 in Fig. 7 will increase due to the coupling and produce a power decrease as $n < 0$, see ΔP_{s2} in Fig. 9. Thus, the active power step response exhibits undershoot behaviors, see ΔP_s in Fig. 9. The active power decrease is mainly caused by the PCC voltage decrease due to lack of reactive power, see ΔU_s in Fig. 9, as there is more reactive power compensation for active power input steps due to the large grid impedance.

In strong grid condition, the grid impedance is small and the coupling between the active power control and AC voltage control is very weak. The AC voltage fluctuation is small enough to be neglected, see ΔU_s in Fig. 9 when SCR=5.

D. Impacts of the SCR and the Active Power on the RHP Zeros

Two cases are presented to investigate the impacts of the SCR and the active power on the existence of RHP zeros of the grid-tied VSC for the $P_s^* \sim P_s$ input-output pair. In the first case, we decrease the SCR from 1.4 to 1.1 when the VSC injects the same rated active power to the AC grid. In the second case, we increase the active power from 0.7 p.u. to 1 p.u. when the VSC connects to a weak-grid with SCR=1.1. The other parameters are the same with those in Table III. The values of the zeros are shown in Fig. 10 and Fig. 11.

Fig. 10 shows that when SCR decreases, i.e., X_g increases, the zeros will move toward the right half plane. When SCR = 1.3 or below with P_s = 1 p.u., the VSC system has two non-real RHP non-minimum-phase zeros indicating that the non-minimum-phase phenomena emerge, which is consistent with the analysis in Section II.

Fig. 11 shows that when P_s increases, the zeros will move toward the right half plane. When P_s is above 0.8 p.u. with SCR = 1.1, the grid-tied VSC system has two non-real RHP non-minimum-phase zeros and becomes a non-minimum-phase system.

Fig. 12 presents G_{PC0}'s Bode plots of the cases in Fig. 10 and Fig. 11. And ω_{c1}, ω_{c2}, ω_{c3} and ω_{c4} are the gain-crossover frequencies, and φ_{c1}, φ_{c2}, φ_{c3} and φ_{c4} are the phase values at the corresponding gain-crossover frequencies. It can be seen from Fig. 12 that the open-loop transfer function G_{PC0} has a larger phase delay when the system has RHP zeros.

It is well known that the VSC system is stable if and only if $\gamma_c = \varphi_c - (-180°) > 0$ satisfies, where γ_c is the phase margin at ω_c. Thus, the large phase delay of the RHP zeros will decrease the phase margin of the weak-grid-tied VSC system, making it difficult to achieve an acceptable dynamic performance.

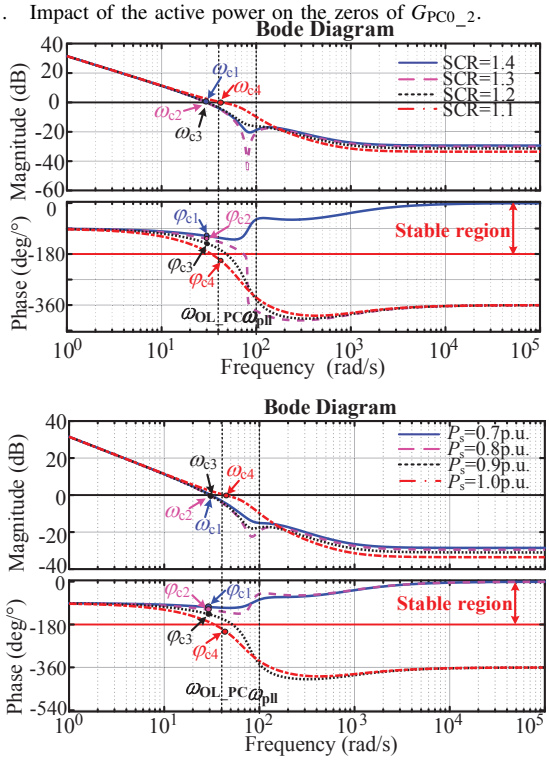

Fig. 12. Bode plots of G_{PC0} with varying SCR and varying active power.

E. Impacts of Control Parameters on the RHP Zeros and Guidance for the Dynamic Performance Improvement

When tuning the converter controller gains, the effect of the non-minimum phase zeros should be taken into account as they impose a limitation on the converter response. According to [8], to ensure an acceptable phase margin, the bandwidth of the non-minimum-phase system should satisfy

$$\omega_b < \frac{|z_i|}{2}, i = 1, 2. \tag{20}$$

where, z_i (i=1,2) is the RHP zero. It is possible to establish a relationship between the zeros and the PLL bandwidth. Table II presents the RHP zeros of G_{PC0} for different PLL's bandwidth and AC voltage control's bandwidth. Table II shows that the RHP zeros satisfy

$$|z_i| = k\omega_{pll}. \tag{21}$$

where k is a coefficient that approximately equals to 1. Fig. 12 shows that G_{PC0} has a largest phase decrease slope at the frequency of ω_{pll}, which also indicates that $|z_i| \approx \omega_{pll}$ satisfies. By combining (20) and (21), the bandwidth of the

TABLE II
RHP ZEROS WITH DIFFERENT CONTROL PARAMETERS

ACvoltage control/(rad/s)	PLL/(rad/s)	RHP zeros z_i	$\lvert z_i\rvert$	$k=\lvert z_i\rvert/\omega_{\text{pll}}$
$2\pi6$	$2\pi16$	70.27±j29.5	76	0.78
$2\pi6$	$2\pi14$	59.85±j37.3	70.52	0.8
$2\pi6$	$2\pi12$	49.39±j41.34	64.4	0.85
$2\pi11$	$2\pi16$	55.18±j78.8	96.2	0.96
$2\pi11$	$2\pi14$	45.22±j76.29	88.68	1.01
$2\pi11$	$2\pi12$	35.20±j72.55	80.64	1.07
$2\pi16$	$2\pi16$	40.86±j101.62	109.53	1.09
$2\pi16$	$2\pi14$	31.35±j95.68	100.69	1.14
$2\pi16$	$2\pi12$	21.79±j88.6	91.24	1.21

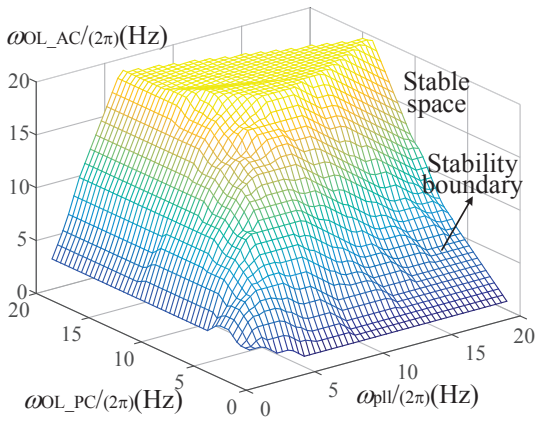

Fig. 13. The stable space concerning the three control parameters with SCR=1.1.

non-minimum-phase system should satisfy

$$\omega_{\text{b}} < \frac{k\omega_{\text{pll}}}{2}. \tag{22}$$

Also, it can be seen from Fig. 12 and (15) that the gain-crossover frequencies satisfy $\omega_{\text{b}} \approx \omega_{ci} \approx \omega_{\text{OL\_PC}}, (i = 1,2,3,4)$. Thus, it yields

$$\omega_{\text{OL\_PC}} < \frac{k\omega_{\text{pll}}}{2}. \tag{23}$$

From Table II and (23), a larger AC voltage control's bandwidth and a larger PLL's bandwidth can help to ensure an acceptable phase margin when an active power control's bandwidth is given. Equation (23) offers a lower limit constraint for the bandwidth selection of the PLL.

F. Stable Space Concerning the Control Parameters

A sensitivity analysis is performed to determine the stability boundaries concerning the three controllers bandwidth under discussion, the bandwidth of the PLL (denoted by ω_{pll}), the bandwidth of the AC active power control (denoted by $\omega_{\text{OL\_PC}}$), and the bandwidth of the AC voltage control (denoted by $\omega_{\text{OL\_AC}}$). A 3-D space is considered with ω_{pll}, $\omega_{\text{OL\_PC}}$ and $\omega_{\text{OL\_AC}}$ all ranging from 2π to $2\pi20$ rad/s, and 3-D plots are presented to show the stable spaces for different SCRs. $2\pi20$ rad/s is adopted as the PLL's bandwidth is usually around $2\pi20$ rad/s [1].

Fig. 13 shows the stable boundaries in the above cube when SCR=1.1. The dots above the stable boundaries in the cube correspond to stable systems, while the system is unstable if the combination of whose three parameters are below the

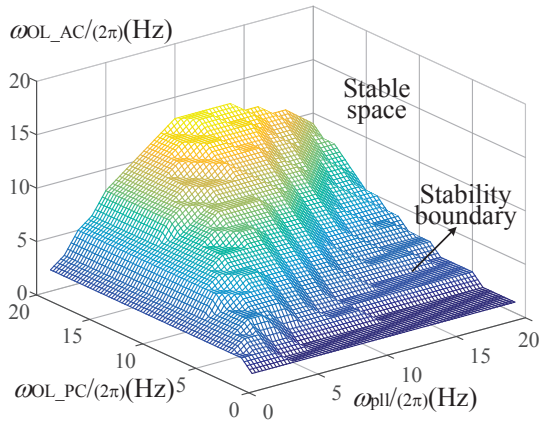

Fig. 14. The stable space concerning the three control parameters with SCR=1.2.

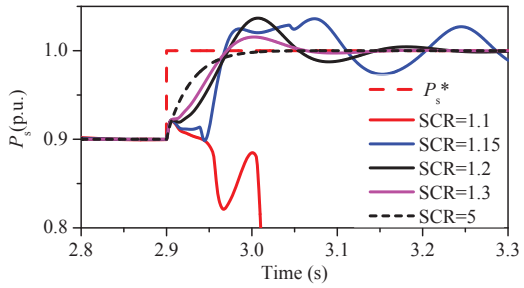

Fig. 15. Time-domain simulation results with SCR=1.1, 1.2, 1.3, 1.4 and 5 when $\omega_{\text{pll}}/(2\pi)$=16 Hz, $\omega_{\text{OL\_AC}}/(2\pi)$=6 Hz, $\omega_{\text{OL\_PC}}/(2\pi)$=6 Hz.

stable boundaries. It is noted that we only examine the stable space within the 3-D cube and that there may exist stable spaces outside. As the SCR can change in a real grid, we also sweep the SCR to analyze the system sensitivity to different parameters under different SCRs. Similarly, Fig. 14 presents the stable space when SCR=1.2. It can be seen that the stable space sketched by the three control parameters contracts when the SCR decreases. This means that some control parameters no longer ensure the system stability when the SCR becomes small. Thus, the parameters need to be re-tuned for smaller SCRs.

It can also be seen from Fig. 13 and Fig. 14 that the stability boundary varies continuously and slowly along the axis of $\omega_{\text{OL\_PC}}$. While, it varies steeply along the axis of ω_{pll}, indicating that the system's stability is more sensitive to the PLL's bandwidth.

V. SIMULATION RESULTS

In this section, we perform time-domain simulations for the cases in Section IV-D and IV-E in MATLAB/Simulink to validate the efficacy of the analysis and the guidance for the performance improvement. A detailed model in Fig. 1 considering the inner current loop is used. The parameters in Table III are adopted.

A. Impacts of the SCR and the Active Power

Fig. 15 shows the time-domain simulation results of the first case for the input-output pair $P_{\text{s}}^* \sim P_{\text{s}}$, with SCR=1.1, 1.2, 1.3, 1.4 and 5. The active power reference P_{s}^* steps from 0.9 p.u. to 1.0 p.u. at 2.9 s. We can see that the step

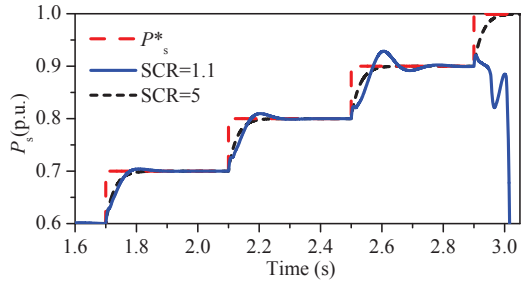

Fig. 16. Time-domain simulation results with P_s=0.7, 0.8, 0.9 and 1.0p.u.when SCR=1, $\omega_{pll}/(2\pi)$=16 Hz, $\omega_{OL\_AC}/(2\pi)$=6 Hz, $\omega_{OL\_PC}/(2\pi)$=6 Hz.

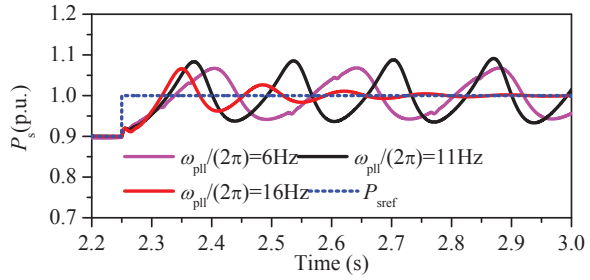

Fig. 17. Time-domain simulation results with $\omega_{pll}/(2\pi)$=6, 11 and 16 Hz when SCR=1.1, $\omega_{OL\_AC}/(2\pi)$=11 Hz, $\omega_{OL\_PC}/(2\pi)$=6 Hz.

responses for SCR=1.1, 1.2, and 1.3 have dips before they first get to the reference, indicating non-minimum-phase systems. While, the non-minimum-phase phenomena are not observed for SCR=1.4 and 5. We can also see that the system becomes unstable when SCR=1.1. Although the system is stable when SCR equals to 1.2 or 1.3, its step response is slower.

Fig. 16 shows the time-domain simulation results of the second case for the input-output pair $P_s^* \sim P_s$. The active power reference P_s^* has a series of reference step changes from 0.6 p.u. to 1.0 p.u. at 1.7 s, 2.1 s, 2.5 s, and 2.9 s, respectively. We can see that the undershoot behavior occurs when the active power increases to 0.9 p.u. from 0.8 p.u.. It can also be seen that the system becomes unstable when the active power reference steps from 0.9 p.u. to 1.0 p.u., with the active power decreasing continuously. The time-domain simulation results are consistent with the conclusions generated in Section IV-D.

B. Impacts of Control Parameters on the Dynamic Performance

According to equation (23) in Section IV-E and Table III, when $\omega_{OL\_PC}/(2\pi)$=6 Hz, $\omega_{pll}/(2\pi)$>12 Hz should be satisfied to ensure the system an acceptable system phase margin. Fig. 17 shows the time-domain simulation results of the case for the input-output pair $P_s^* \sim P_s$, with $\omega_{pll}/(2\pi)$=6, 11, and 16 Hz when $\omega_{OL\_AC}/(2\pi)$=11 Hz. The active power reference P_s^* steps from 0.9 p.u. to 1.0 p.u. at 2.25 s. It can be seen that the step response is stable when $\omega_{pll}/(2\pi)$=16 Hz and is unstable when $\omega_{pll}/(2\pi)$=6, 11 Hz, which is consistent with the analysis.

TABLE III
PARAMETERS OF THE VSC SYSTEM

Parameters	Unit	Value
Rated power/voltage	MW/kV	300/110
SCR,R_g,L_g,frequency	p.u.,Ω,mH,Hz	1.1, 0.367, 116.7,50
R_{eq},L_{eq}	Ω, mH	0.403, 25.7
ω_{pll},k_{p_pll},k_{i_pll}	rad/s, rad/(V · s), rad/(V · s^2)	2π16, 1.6×10^{-3}, 0.1125
ω_{OL_PC},k_{p_PC},k_{i_PC}	rad/s, A/W, A/(W · s)	2π6, 3.56×10^{-7}, 2.8×10^{-4}
ω_{OL_AC},k_{p_AC},k_{i_AC}	rad/s, A/V, A/(V · s)	2π6, 1.3×10^{-3}, 1.028
ω_{CL}, k_{p_cl}, k_{i_cl}	rad/s, Ω, V/(A · s)	2π125, 20.17, 316.78
P_s,U_s	p.u., p.u.	1.0, 1.0
ζ,T_d	1, s	0.707, 4.0×10^{-4}

Fig. 18. The RTDS used in the experiment.

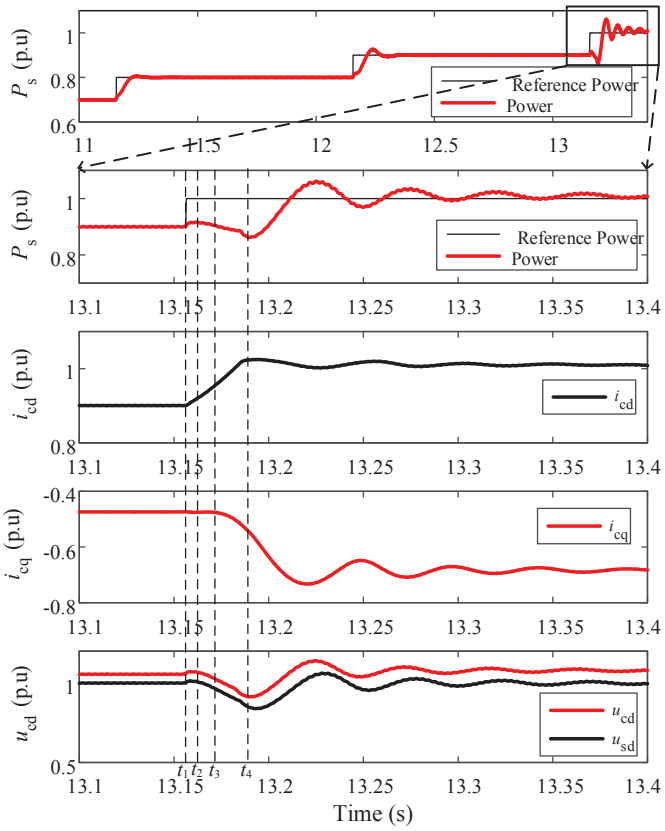

Fig. 19. The undershoot behavior in the RTDS experiment when SCR=1.15, $\omega_{pll}/(2\pi)$=16 Hz, $\omega_{OL\_AC}/(2\pi)$=11 Hz, $\omega_{OL\_PC}/(2\pi)$=6 Hz.

VI. REALTIME VALIDATION

In this section, the results obtained using a Real Time Digital Simulator (RTDS) are provided to validate the analysis

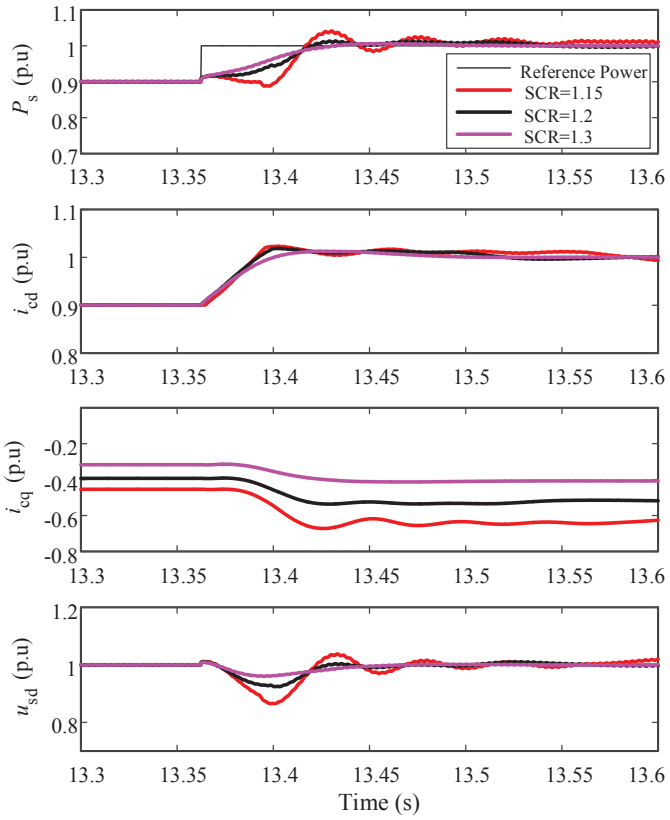

Fig. 20. RTDS experiment results with SCR=1.15, 1.2, 1.3 when $\omega_{pll}/(2\pi)$=16 Hz, $\omega_{OL\_AC}/(2\pi)$=11 Hz, $\omega_{OL\_PC}/(2\pi)$=6 Hz.

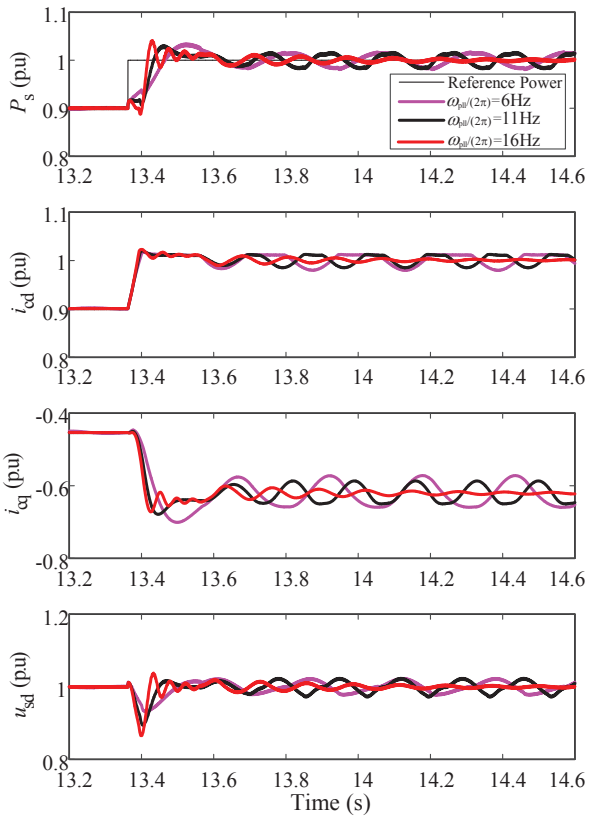

Fig. 21. RTDS experiment results with $\omega_{pll}/(2\pi)$=6, 11 and 16 Hz when SCR=1.1, $\omega_{OL\_AC}/(2\pi)$=11 Hz, $\omega_{OL\_PC}/(2\pi)$=6 Hz.

of the non-minimum-phase phenomenon and impacts of the SCR and the control parameters. The parameters in Table III are used. Fig. 18 shows the RTDS used in the experiment.

A. Undershoot Phenomenon of the Active Power Response

To verify the analysis in Section IV-C, Fig. 19 presents the active power step responses from 0.7 p.u. to 0.8 p.u., 0.9 p.u. and 1 p.u. when SCR=1.15, $\omega_{OL\_AC}/(2\pi)$=11 Hz, $\omega_{OL\_PC}/(2\pi)$=6 Hz and $\omega_{pll}/(2\pi)$=16 Hz. The undershoot behavior when the active power steps from 0.9 p.u. to 1 p.u. can be observed and described as follows.

When the P_s^* steps from 0.9 p.u. to 1.0 p.u., the output voltage u_{cd} of the VSC increases instantaneously to force the active current i_{cd} to increase during (t_1, t_2), which leads to the increase of the PCC voltage u_{sd} and the active power. Then, during (t_2, t_3), the increase of the active current leads to a voltage drop over the grid impedance especially in weak grid conditions, which leads to the decrease of the PCC voltage u_{sd}. The active power also decreases. During (t_3, t_4) in Fig. 19, the active current i_{cd} continues to increase and the PCC voltage continues to decrease. The AC voltage control of the VSC begins to generate a reactive current i_{cq} to prevent the decrease of the AC voltage. At the time instant of t_4, the active current reaches its reference value and PCC voltage u_{sd} almost reaches its minimum value. Then the reactive current i_{cq} continues to increase the PCC voltage and the active power till the system converges to a new steady state.

B. Impacts of the SCR

Fig. 20 shows the RTDS experiment results for the input-output pair P_s^* ~ P_s, with SCR=1.15, 1.2, 1.3 when $\omega_{OL\_AC}/(2\pi)$=11 Hz, $\omega_{OL\_PC}/(2\pi)$=6 Hz and . The active power reference P_s^* steps from 0.9 p.u. to 1.0 p.u. when t=13.37 s. We can see that the step responses for SCR=1.15 have obvious dips before getting to the reference, indicating non-minimum-phase systems. While, the power and PCC voltage dips for SCR=1.2 and 1.3 are not as deep as SCR=1.15. We can also see that smaller the SCRs can slow the step response.

C. Impacts of the PLL Bandwidth

Fig. 21 shows the RTDS experiment results for the input-output pair P_s^* ~ P_s, with $\omega_{pll}/(2\pi)$=6, 11, and 16 Hz when SCR=1.15, $\omega_{OL\_AC}/(2\pi)$=11 Hz and $\omega_{OL\_PC}/(2\pi)$=6 Hz. The active power reference P_s^* steps from 0.9 p.u. to 1.0 p.u. when t=13.37 s. It can be seen that the step response converges when $\omega_{pll}/(2\pi)$= 16 Hz while has oscillations when $\omega_{pll}/(2\pi)$=6, 11 Hz, verifying that a larger PLL's bandwidth can improve dynamic performance when the active power control's bandwidth is given.

VII. Conclusions

In this paper, the non-minimum-phase phenomenon of weak-grid-tied VSCs is investigated. Based on the open-loop transfer function of a specific SISO input-output pair P_s^* ~ P_s, the RHP zeros are firstly examined. We find that large grid

impedance and large injected active power are the physical origins of the non-minimum-phase zeros. The non-minimum-phase system has a large phase delay and presents very poor dynamic performances as the phase margin is reduced and the control bandwidth is limited by the RHP zeros. It is concluded that the RHP zeros will limit the minimum PLL bandwidth. Simulink simulations and RTDS experiments are performed to validate the theoretical analysis. The time-domain simulation and RTDS experiments results agree with the theoretical predictions, which verifies the analysis of this paper and confirms the importance of non-minimum-phase zeros in the stability of weak-grid-tied converters.

Appendix

A. Modelling of the Plant

By applying KVL over the grid equivalent impedance in the frame of the grid, we obtain

$$\left[\begin{array}{cc} \frac{-R_{\mathrm{g}}}{L_{\mathrm{g}}} & \omega_1 \\ -\omega_1 & \frac{-R_{\mathrm{g}}}{L_{\mathrm{g}}} \end{array}\right]\left[\begin{array}{c} i_{\mathrm{cd}} \\ i_{\mathrm{cq}} \end{array}\right]+\frac{1}{L_{\mathrm{g}}}\left[\begin{array}{c} u_{\mathrm{sd}}-u_{\mathrm{gd}} \\ u_{\mathrm{sq}}-u_{\mathrm{gq}} \end{array}\right]=\left[\begin{array}{c} 0 \\ 0 \end{array}\right]. \tag{24}$$

By applying KVL over the equivalent impedance between the VSC and the PCC in the grid's frame, we obtain

$$\left[\begin{array}{cc} \frac{-R_{\mathrm{eq}}}{L_{\mathrm{eq}}} & \omega_1 \\ -\omega_1 & \frac{-R_{\mathrm{eq}}}{L_{\mathrm{eq}}} \end{array}\right]\left[\begin{array}{c} i_{\mathrm{cd}} \\ i_{\mathrm{cq}} \end{array}\right]+\frac{1}{L_{\mathrm{eq}}}\left[\begin{array}{c} u_{\mathrm{cd}}-u_{\mathrm{sd}} \\ u_{\mathrm{cq}}-u_{\mathrm{sq}} \end{array}\right]=\left[\begin{array}{c} 0 \\ 0 \end{array}\right], \tag{25}$$

where R_{eq} and L_{eq} are the equivalent resistor and inductor between the VSC and the PCC respectively.

The magnitude of the PCC voltage U_{s} and the active/reactive power injected to the power grid can be described by

$$\left\{\begin{array}{l} U_{\mathrm{s}}=\sqrt{u_{\mathrm{sd}}^2+u_{\mathrm{sq}}^2} \\ P_{\mathrm{s}}=1.5\left(u_{\mathrm{sd}}i_{\mathrm{cd}}+u_{\mathrm{sq}}i_{\mathrm{cq}}\right), Q_{\mathrm{s}}=1.5\left(u_{\mathrm{sq}}i_{\mathrm{cd}}-u_{\mathrm{sd}}i_{\mathrm{cq}}\right) \end{array}\right. . \tag{26}$$

B. Modelling of the VSC Control System

In Fig. 4, the mapping relation of one variable in the two different frames is $F_{\mathrm{dq}}^{\mathrm{cf}}=\boldsymbol{T}_{\mathrm{dq2dqcf}}F_{\mathrm{dq}}$,

where F denotes u_{s}, u_{c}, u_{g} or i_{c}, the superscript "cf" denotes that the variable is in the the control system's dq frame, and $\boldsymbol{T}_{\mathrm{dq2dqcf}}$ can be written as

$$\boldsymbol{T}_{\mathrm{dq2dqcf}}=\left[\begin{array}{cc} \cos\theta_{\mathrm{pll}} & \sin\theta_{\mathrm{pll}} \\ -\sin\theta_{\mathrm{pll}} & \cos\theta_{\mathrm{pll}} \end{array}\right], \tag{27}$$

where θ_{pll} is the initial phase of the PCC voltage calculated by PLL. Each part of the control system in Fig. 1 can be demonstrated in detail as follows.

1) *PLL*: The PLL shown in Fig. 1 can be described by

$$\theta=\left(G_{\mathrm{PI-pll}}u_{\mathrm{sq}}^{\mathrm{cf}}+\omega_1\right)\frac{1}{s}, \tag{28}$$

where $G_{\mathrm{PI-pll}}$ is the PI controller and can be written as

$$G_{\mathrm{PI-pll}}=k_{\mathrm{p\_pll}}\left(1+\frac{1}{sT_{\mathrm{i\_pll}}}\right), \tag{29}$$

where $k_{\mathrm{p\_pll}}$ and $T_{\mathrm{i\_pll}}$ are the proportional coefficient and the integral time constant of $G_{\mathrm{PI-pll}}$. They can be obtained by $k_{\mathrm{p\_pll}}=2\zeta\omega_{\mathrm{pll}}/u_{\mathrm{sd0}}$, $T_{\mathrm{i\_pll}}=2\zeta/\omega_{\mathrm{pll}}$. And ω_e can be described by $\omega_{\mathrm{e}}=G_{\mathrm{PI-pll}}(s)u_{\mathrm{sq}}^{\mathrm{cf}}$.

2) *Outer Loop Control*: The outer loop can be described by

$$i_{\mathrm{cd}}^{\mathrm{cf}*}=G_{\mathrm{PC}}(P_{\mathrm{s}}^{*}-P_{\mathrm{s}}^{\mathrm{cf}}), i_{\mathrm{cq}}^{\mathrm{cf}*}=G_{\mathrm{AC}}(U_{\mathrm{s}}^{*}-U_{\mathrm{s}}^{\mathrm{cf}}), \tag{30}$$

where G_{PC} and G_{AC} can be described by

$$G_{\mathrm{PC}}=k_{\mathrm{p\_PC}}\left(1+\frac{1}{sT_{\mathrm{i\_PC}}}\right), G_{\mathrm{AC}}=-k_{\mathrm{p\_AC}}\left(1+\frac{1}{sT_{\mathrm{i\_AC}}}\right), \tag{31}$$

where $k_{\mathrm{p\_PC}}$ and $T_{\mathrm{i\_PC}}$ are the proportional coefficient and integral time constant of G_{PC} respectively, and $k_{\mathrm{p\_AC}}$ and $T_{\mathrm{i\_AC}}$ are the proportional coefficient and integral time constant of G_{AC} respectively. They can be obtained by $T_{\mathrm{i\_PC}}=T_{\mathrm{i\_AC}}=1/\omega_{\mathrm{CL}}$, $k_{\mathrm{p\_PC}}=\omega_{\mathrm{OL\_PC}}T_{\mathrm{i\_PC}}/(1.5u_{\mathrm{sm}})$, $k_{\mathrm{p\_AC}}=\omega_{\mathrm{OL\_AC}}T_{\mathrm{i\_PC}}/X_{\mathrm{g}}$, where u_{sm} is the magnitude of the grid's phase voltage.

3) *Inner Loop Control*: According to the assumption, the inner current loop can be described by

$$i_{\mathrm{cd}}^{\mathrm{cf}}=i_{\mathrm{cd}}^{\mathrm{cf}*}, i_{\mathrm{cq}}^{\mathrm{cf}}=i_{\mathrm{cq}}^{\mathrm{cf}*}, \tag{32}$$

where the superscript of * means the reference value.

References

[1] J. Hu, Q. Hu, B. Wang, H. Tang, and Y. Chi, "Small signal instability of PLL-synchronized type-4 wind turbines connected to high-impedance AC grid during LVRT," *IEEE Trans. Energy Conv.*, vol. 31, no. 4, pp. 1676–1687, Dec. 2016.

[2] G. Li, J. Liang, F. Ma, C. E. Ugalde-Loo, and H. Liang, "Analysis of single-phase-to-ground faults at the valve-side of HB-MMCs in HVDC systems," *IEEE Trans. Ind. Electron.*, vol. 66, no. 3, pp. 2444–2453, Mar. 2019.

[3] A. Egea-Alvarez, S. Fekriasl, F. Hassan, and O. Gomis-Bellmunt, "Advanced vector control for voltage source converters connected to weak grids," *IEEE Trans. Power Sys.*, vol. 30, no. 6, pp. 3072–3081, Nov. 2015.

[4] J. Z. Zhou, H. Ding, S. Fan, Y. Zhang, and A. M. Gole, "Impact of Short-Circuit Ratio and Phase-Locked-Loop Parameters on the Small-Signal Behavior of a VSC-HVDC Converter," *IEEE Trans. Power Del.*, vol. 29, no. 5, pp. 2287–2296, Oct. 2014.

[5] L. Fan and Z. Miao, "Wind in weak grids: 4 hz or 30 hz oscillations?," *IEEE Trans. Power Sys.*, vol. 33, no. 5, pp. 5803–5804, Sep. 2018.

[6] L. Xu and L. Fan, "Impedance-based resonance analysis in a VSC-HVDC system," *IEEE Trans. Power Del.*, vol. 28, no. 4, pp. 2209–2216, Oct. 2013.

[7] Y. Li, L. Fan, and Z. Miao, "Wind in Weak Grids: Low-Frequency Oscillations, Subsynchronous Oscillations, and Torsional Interactions," *IEEE Trans. Power Sys.*, vol. 35, no. 1, pp. 109–118, Jan. 2019.

[8] S. Skogestad and I. Postlethwaite, *Multivariable feedback control: analysis and design*, vol. 2. Wiley New York, 2007.

[9] L. Zhang, *Modeling and control of VSC-HVDC links connected to weak AC systems*. PhD thesis, KTH, Stockholm, Sweden, 2010.

[10] J. Sun, "Impedance-based stability criterion for grid-connected inverters," *IEEE Trans. Power Electron.*, vol. 26, no. 11, pp. 3075–3078, Nov. 2011.

[11] M. Cespedes and J. Sun, "Impedance modeling and analysis of grid-connected voltage-source converters," *IEEE Trans. Power Electron.*, vol. 29, no. 3, pp. 1254–1261, Mar. 2014.

[12] A. G. MacFarlane and I. Postlethwaite, "The generalized Nyquist stability criterion and multivariable root loci," *Int. J. Contr.*, vol. 25, no. 1, pp. 81–127, Mar. 2007.

[13] Y. Huang, X. Yuan, J. Hu, and P. Zhou, "Modeling of VSC connected to weak grid for stability analysis of DC-link voltage control," *IEEE J. Emerg. Sel. Topics Power Electron.*, vol. 3, no. 4, pp. 1193–1204, Dec. 2015.

[14] I. Canay, "A novel approach to the torsional interaction and electrical damping of the synchronous machine Part I: Theory," *IEEE Trans. Power App. and Sys.*, no. 10, pp. 3630–3638, Oct. 1982.

[15] L. Fan, "Modeling type-4 wind in weak grids," *IEEE Trans. Sustain. Energy*, vol. 10, no. 2, pp. 853–864, Apr. 2019.

[16] C. Guo, W. Liu, C. Zhao, and R. Iravani, "A frequency-based synchronization approach for the VSC-HVDC station connected to a weak AC grid," *IEEE Trans. Power Del.*, vol. 32, no. 3, pp. 1460–1470, Jun. 2017.

[17] G. Wu, J. Liang, X. Zhou, Y. Li, A. Egea-Alvarez, G. Li, H. Peng, and X. Zhang, "Analysis and design of vector control for VSC-HVDC connected to weak grids," *CSEE J. Power and Energy Sys.*, vol. 3, no. 2, pp. 115–124, Jun. 2017.
[18] Y. Li, X. Wang, J. Guo, H. Wu, B. Zhao, S. Wang, G. Wu, and T. Wang, "PLL Synchronization Stability Analysis of MMC-Connected Wind Farms under High-Impedance AC Faults," *IEEE Trans. Power Sys.*, early access, 2020. https://doi.org/10.1109/TPWRS.2020.3025917.
[19] H. Zhang, L. Harnefors, X. Wang, H. Gong, and J.-P. Hasler, "Stability analysis of grid-connected voltage-source converters using SISO modeling," *IEEE Trans. Power Electron.*, vol. 34, no. 8, pp. 8104–8117, Aug. 2019.
[20] G. Wu, H. Sun, X. Zhang, A. Egea-Alvarez, B. Zhao, S. Xu, S. Wang, and X. Zhou, "Parameter design oriented analysis of the current control stability of the weak-grid-tied VSC," *IEEE Trans. Power Del.*, early access, 2020. https://doi.org/10.1109/TPWRD.2020.3009517.
[21] J. Hu, Y. Huang, D. Wang, H. Yuan, and X. Yuan, "Modeling of grid-connected DFIG-based wind turbines for DC-link voltage stability analysis," *IEEE Trans. Sustain. Energy*, vol. 6, no. 4, pp. 1325–1336, Oct. 2015.
[22] J. B. Hoagg and D. S. Bernstein, "Nonminimum-phase zeros-much to do about nothing-classical control-revisited part II," *IEEE Control Syst. Mag.*, vol. 27, no. 3, pp. 45–57, Jun. 2007.

Guanglu Wu received the B.Eng. degree from North China Electric Power University, Beijing, China, in 2012 and the Ph.D. degree from China Electric Power Research Institute, Beijing, China, in 2018, both in electrical engineering. He is currently working as an engineer in the Power System Department of China Electric Power Research Institute, Beijing, China.

His current research interests include VSC-HVDC, DC grid, power converter control and stability analysis of the power system with power electronic devices.

Bing Zhao received the B.Eng. and Master degree from Xi'an university of technology, Xi'an, China, in 2003 and 2006, respectively, both in electrical engineering. He received the Ph.D. degree from China Electric Power Research Institute (CEPRI), Beijing, China, in 2009, in electrical engineering. He is currently working as a professor of electrical engineering in the Power System Department of CEPRI, Beijing, China.

His research interests include power system stability analysis and control, load modelling, renewable power generation and integration, and operation and control of the DC grid.

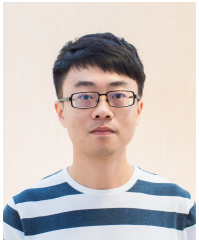

Xi Zhang received the B.Eng. degree from Beijing Jiaotong University, Beijing, China, in 2013 and the Ph.D. degree from Hong Kong Polytechnic University, Hong Kong, in 2017, both in electrical engineering. He worked as a postdoc in the Power System Department of China Electric Power Research Institute, Beijing, China from 2018 to 2019. Currently, he is an assisant professor in School of Automation, Beijing Institute of Technology, Beijing, China since 2020.

His research interests include complexity, resilience and stability analysis of the power system with high penetrations of power electronic devices.

Shanshan Wang received the B.Eng. and Master degree from Shandong university, Jinan, China, in 2003 and 2006, respectively, both in electrical engineering. She received the Ph.D. degree from China Electric Power Research Institute (CEPRI), Beijing, China, in 2011, in electrical engineering. She is currently working as a senior engineer in the Power System Department of CEPRI, Beijing, China.

Her research interests include analysis and design of VSC-HVDC, power system stability analysis and control and operation and control of the DC grid.

Agustí Egea-Àlvarez (S'12–M'14) obtained his B-Sc, MSc and Ph.D. from the Technical University of Catalonia in Barcelona in 2008, 2010 and 2014 respectively. In 2015 he was a Marie Curie fellow in the China Electric Power Research Institute (CEPRI). In 2016 he joined Siemens Gamesa as converter control engineer working on grid forming controllers and alternative HVDC schemes for offshore wind farms. He is a member of IEEE, IET and has been involved in several CIGRE and ENTSO-E working groups. Currently, Dr Agust Egea-lvarez is Strathclyde Chancellors fellow (Lecturer) at the electronic & electrical engineering department and member of the PEDEC (Power Electronics, Drives and Energy Conversion) group since 2018.

His current research interests include control and operation of high-voltage direct current systems, renewable generation systems, electrical machines and power converter control.

Yuanyuan Sun (M14) received the B.S. and Ph.D. degrees in electrical engineering from the School of Electrical Engineering, Shandong University, Jinan, China, in 2003 and 2009, respectively. She is currently an Associate Professor with the School of Electrical Engineering, Shandong University, Jinan, P. R. China.

Her current research interests include harmonic modeling, harmonic contribution determination, and active distribution system analysis.

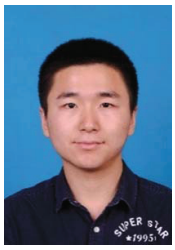

Yingbiao Li received the BEng degree from Wuhan University, Wuhan, China, in 2014, the Master and Ph.D. degree from China Electric Power Research Institute, Beijing, China, in 2017 and 2020, both in electrical engineering. He is currently a post Ph.D. in the School of Electrical and Electronic Engineering, Huazhong University of Science and Technology, Wuhan, China.

His research interests include VSC-HVDC, DC grid and stability analysis of the power system with high penetrations of power electronic devices.

Deyang Guo received the B.Sc. degree from North China Electric Power University, Beijing, China, in 2015, the Ph.D degree from University of Strathclyde, Glasgow, U.K, in 2020. He is currently working as an engineer in China Electric Power Research Institute, Beijing, China.

His current research interests include power electronics, modelling and control of HVDC systems.

Xiaoxin Zhou (F'96–LF'10) graduated from Tsinghua University, Beijing, China, in 1965. He is the Honorary President of China Electric Power Research Institute (CEPRI), academician of Chinese Academy of Sciences, and Fellow of IEEE. In 2008, he received the IEEE Power & Energy Society Nari Hingorani FACTS Award.

Currently, he serves as the Editor-in-Chief for the *CSEE Journal of Power and Energy Systems* since 2015. His main research interests include power system analysis and control, power system digital simulation, Flexible AC Transmission System (FACTS), and integration of large scale renewable power generation.